Computers and Structures 238 (2020) 106297

Contents lists available at ScienceDirect

Computers and Structures

journal homepage: www.elsevier.com/locate/compstruc

Automated optimization-based generation and quantitative evaluation of Strut-and-Tie models

Yi Xia [a,b,*], Matthijs Langelaar [b], Max A.N. Hendriks [a,c]

[a] Faculty of Civil Engineering & Geosciences, Delft University of Technology, Delft, Netherlands
[b] Faculty of Mechanical, Maritime and Materials Engineering, Delft University of Technology, Delft, Netherlands
[c] Department of Structural Engineering, Norwegian University of Science and Technology (NTNU), Trondheim, Norway

ARTICLE INFO

Article history:
Received 18 February 2020
Accepted 15 May 2020
Available online 28 June 2020

Keywords:
Reinforced concrete structure
Strut-and-Tie
Automatic generation
Integrated optimization
Topology optimization
Nonlinear Finite Element Analysis

ABSTRACT

Strut-and-Tie modelling (STM) is a well-known approach to design D-regions in reinforced concrete structures. Because the STM method is based on lower-bound analysis, finding a suitable truss-analogy model is the most important aspect to guarantee good structural and economic performance of a resulting design. Continuum topology optimization (TO) methods have been studied for two decades to solve this problem. However, while these studies provide inspiration to designers, they lack the capability to automatically generate valid truss-analogy models as needed in the STM method. In order to prevent manual interpretation and automatically generate suitable STM models for various D-regions, a method is proposed for the generation of optimization-based STM (OPT-STM) models. The proposed method includes three phases: the TO phase, the topology extraction phase and the shape optimization phase. Next, in order to evaluate the effectiveness of the generated OPT-STM models, an evaluation using Nonlinear Finite Element Analysis (NLFEA) is performed to analyze the performance of STM models. For two D-region problems, two OPT-STM models and 11 manually constructed STM models from literature are evaluated, and their performance is compared and discussed, demonstrating the validity and effectiveness of the proposed automated generation method.

1. Introduction

The Strut-and-Tie modelling (STM) method is an effective tool for engineers to design disturbed regions (so-called D-regions) of reinforced concrete (RC) structures. The STM method as a truss analogy method was first generalized as a consistent RC structure design method by Schlaich et al. [52] and Schlaich and Schafer [51]. It uses truss analogy models to indicate force and stress distributions in D-regions, and is based on the limit lower-bound theory of plasticity [46,62]. The method requires axial force equilibrium while neglecting strain compatibilities [44,24]. The design process of applying STM methods is convenient for engineers in practice, and resulting designs are conservative, assuming sufficient ductility. Various investigations of the STM method have been conducted by engineers and researchers in past decades, and results have been implemented in design codes worldwide, e.g. British Standards [16], Canadian Standards [21], code requirements from the American Concrete Institute [2], fib Model Code for Concrete Structures 2010 [27], the American Association of State Highway and Transportation Officials [1] and Eurocode [17].

In STM analysis, the load-to-support transfer mechanisms of design problems are represented using truss analogy models. Axial equilibrium forces are calculated, and model members with compressive and tensile forces are categorized as struts and ties respectively. The corresponding dimensioning process and strength checks are carried out for nodes, struts and ties. Regarding the whole process of the STM method, different aspects have been investigated by researchers: 1. In order to predict the ultimate behaviour of concrete structures, concrete cracking and compatibility conditions were implemented in the STM method [34,7,37,69,19]; 2. In order to predict accurate load capacity using the STM method, the ultimate strength and strength factors of struts and nodes under various conditions were investigated [66,54,49,31]; 3. In order to validate the effectiveness and safety of STM designs, experiments of various STM designs for different D-regions were conducted [18,41,38,45,29,35]; 4. In order to facilitate the STM design process in engineering practice, computer STM design tools were developed by researchers to generate various STM models [6,63,56,65,48,64].

* Corresponding author at: Faculty of Civil Engineering & Geosciences, Delft University of Technology, Delft, Netherlands.
E-mail address: y.xia@tudelft.nl (Y. Xia).

https://doi.org/10.1016/j.compstruc.2020.106297
0045-7949/

Among different investigation aspects related to the STM method, finding a suitable truss analogy model is a priority and is one of the most important problems [51]. Based on the lower-bound theory, various models are available and perform differently, however more economical (i.e. less conservative) designs are preferred and can be obtained by using suitable models [24]. Schlaich and Schafer [51] suggested using the load path method or using stress fields obtained through linear finite element analysis (FEA) as inspirations to construct truss analogy models for the STM analysis. However, difficulties of using these methods to generate STM models arise when D-regions become more complex [42]. In order to address this problem and to provide a method for a more generalized treatment of D-regions, topology optimization (TO) methods have been considered. Using TO to find suitable STM models is one of the most popular research directions in this field.

Various investigations using TO in the STM method have been conducted in the past two decades. Biondini et al. [11], Ali and White [3,4], Biondini et al. [12] used ground structure based TO methods to generate truss-analogy models for the STM method. Numerous approaches using continuum TO methods have been explored for the same purpose. Liang et al. [42] firstly used the evolutionary structural optimization (ESO) method for creating STM models from the optimized material layouts. Later on, various other ESO approaches were proposed [30,40,39,5]. Alternatively, for the same problem, Bruggi [13,14] and Jewett and Carstensen [36] used SIMP (solid isotropic material with penalization) TO methods to generate optimized topologies for the STM method, whereas the isoline TO method was used in Victoria et al. [58] and the full-homogenization method was used in Herranz et al. [32]. Apart from using different TO methods, more sophisticated material models were adopted in the TO process: Victoria et al. [58] and Du et al. [23] used bi-modulus material properties for the generation of STM models, Bruggi [15] implemented an energy-based TO approach considering no-tension concrete for deriving STM models. and Gaynor et al. [28] and Jewett and Carstensen [35] considered bi-modulus material properties within a hybrid truss-continuum element formulation for generating optimized material layouts for the STM method.

Despite intensive efforts of using various TO approaches for the STM method, the generated optimized results from these approaches cannot be used as STM models without manual adjustments. Because TO results are continua and STM models are truss analogy models, most approaches can only provide optimized material layouts as inspiration for subsequent manual generation of STM models. Manual and subjective interpretations are required to transform TO results to adequate STM models. Consequently, interpreted STM models show considerable variation. Moreover, the manual interpretation process is impractical and inefficient in engineering practice. This hampers the utilization of TO methods for STM. The problem how to generate STM models directly through the optimization process has thus far not been solved. This problem is first clearly identified and discussed in more depth in our recent review on evaluating TO methods for STM [59]. To our best knowledge, no investigations have been reported that fully address this gap. Thus, automated optimization-based procedures to construct an STM model are highly desired.

In this paper, we therefore propose an automatic generation method for optimization-based STM (OPT-STM) models. The method starts with a design problem which includes the geometry, boundaries and load conditions, and compliance minimization-based topology optimization is conducted for this problem to obtain optimized material layouts. Next, instead of manually interpreting truss-like structures based on TO results, a fully automatic topology extraction method is proposed to replace this manual process. Note that the STM method requires a truss-analogy model satisfying axial-force equilibrium, however the extracted truss-like structures are usually unstable trusses and equilibrium forces cannot be calculated through truss analysis [59]. Consequently, a subsequent shape optimization method is introduced to automatically adjust the extracted truss-like structures to valid STM models, in which axial force equilibrium is satisfied. Moreover, important practical geometrical conditions, such as minimum concrete cover for reinforcement and the member distances to outer surfaces, are included as constraints in the optimization process. The whole generation method is implemented as an integrated and automatic procedure. Thus, the generation method prevents ad-hoc topological changes of TO results commonly applied in manual STM model generations and simplifies the process of generating STM models in engineering practice.

In order to validate the effectiveness of the generated OPT-STM models, an evaluation method is proposed by using Nonlinear Finite Element Analysis (NLFEA). The nonlinear behavior of concrete cracking and crushing and steel yielding and rupturing are considered. This provides more detailed insights to evaluate the performance of STM models. Two typical D-region design problems are investigated. By comparing the evaluation results of the generated OPT-STM models with 11 previously proposed STM models from literature, the effectiveness of the proposed automated generation method is demonstrated. As will be shown, in particular the amount of necessary reinforcement is significantly lower for the OPT-STM designs, while load capacities remain comparable between all models. Note that, in order to avoid subjective manual interventions, reinforcement detailing aspects and constructibility issues after the STM analysis are not considered in the evaluation process.

The remainder of the paper is organized as follows: the novel generation method of optimization-based STM models is introduced in Section 2. The evaluation method for STM models is presented in Section 3. Three aspects of the generation method, including the influence of optimization parameters in the TO process, the merging length in the topology extraction process and the importance of satisfying axial equilibrium forces, are discussed in Section 4. Finally, a comparative evaluation based on two D-region design problems is presented in Section 5 and conclusions are given in Section 6.

2. Automatic generation of optimization-based Strut-and-Tie models

An automatic and integrated generation method is introduced in this section for the generation of OPT-STM models. An example of a D-region design problem (a dapped-end beam with an opening) is used to exemplify the proposed generation method. The geometry, loads and supports of this D-region are shown in Fig. 1. The thickness of this structure is 120mm. The D-region has been experimentally investigated by Oviedo et al. [47]. The

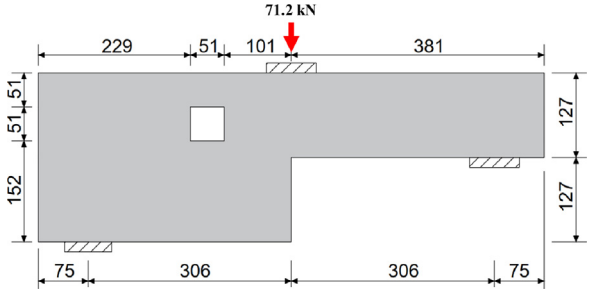

Fig. 1. The dapped-end beam design problem (mm).

proposed method includes three main phases, as shown in the flowchart in Fig. 2:

Topology optimization phase: The compliance minimization-based TO method is adopted for generating optimized material layouts of given design problems. The classical density-based SIMP TO method [10] is used in this paper. The details are introduced in Section 2.1.

Topology extraction phase: A topology extraction method is developed to transform TO continua to truss-like structures. The extracted truss-like structure comprises a network consisting of straight, connected structural members which distributes forces from loads to supports. The detailed procedures of the extraction method are introduced in Section 2.2.

Shape optimization phase: The extracted truss-like structures are usually unstable trusses. Therefore, the equilibrium forces cannot be calculated by truss analysis in most cases. However, the requirement of the axial-force equilibrium state is a prerequisite for using truss analogies in STM models. In Section 2.3, the proposed shape optimization method to generate adequate STM models based on the extracted truss-like structures is presented.

2.1. Topology optimization phase

Since the landmark work by Bendsøe and Kikuchi [9], continuum TO methods have been investigated broadly, and have become powerful and creative approaches for a wide variety structural design applications. Specifically in the conceptual design phase, TO methods provide a systematic procedure to find optimized material distributions of a given domain with specific load and support conditions.

The classical SIMP TO method [10] is adopted here to optimize material distributions of given problems. Note that various other TO methods could be used in this phase, as reviewed in the preceding section. Although we employ a classical TO approach, its main steps are discussed here for completeness; for additional details, the reader is referred to Bendsoe and Sigmund [10]. Topology optimization variables, so called densities $\boldsymbol{\rho}$, are assigned to all elements in the FEM model. Based on FEM analysis results and sensitivity information, densities are updated at each optimization iteration until the process converges.

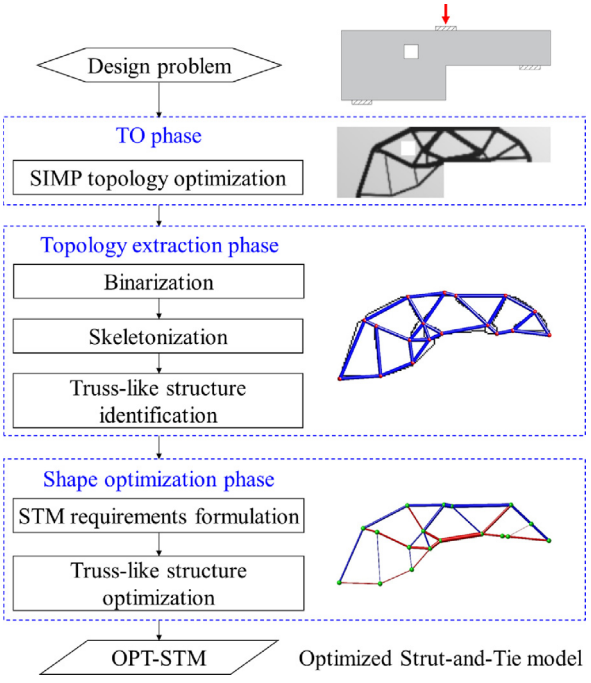

Fig. 2. Flowchart of the OPT-STM generation method.

Based on the SIMP method, the mathematical formulation of the compliance minimization TO problem is:

$$\begin{aligned} \text{minimize}: \quad & C(\boldsymbol{\rho}) = \boldsymbol{F}^{\mathrm{T}}\boldsymbol{U}(\boldsymbol{\rho}) \\ \text{subject to}: \quad & \boldsymbol{K}(\boldsymbol{\rho})\boldsymbol{U} = \boldsymbol{F} \\ & V(\boldsymbol{\rho}) \leqslant \alpha\overline{V} \\ & \boldsymbol{\varepsilon} \leqslant \boldsymbol{\rho} \leqslant \boldsymbol{1} \end{aligned} \tag{1}$$

In this optimization problem, C is the compliance of the structure, $\boldsymbol{F}$ and $\boldsymbol{U}$ are the nodal force vector and the nodal displacement vector respectively. $\boldsymbol{\rho}$ is the density vector which elements are in the range between ε (denoting void) and 1 (solid). The lower limit $\varepsilon$is a small value (10^{-4}) which prevents singularity of $\boldsymbol{K}$, which is the structural stiffness matrix depending on densities $\boldsymbol{\rho}$ as discussed below. $V(\boldsymbol{\rho})$ and $\overline{V}$ are the material volume and the total volume of the full domain respectively. $\alpha \in [0,1]$ is a specific volume fraction for limiting the material utilization of optimized results.

In this paper, conventional four-node bilinear finite elements under plane stress assumption are adopted to perform the finite element analysis in all 2D examples. In the SIMP TO method, the Young's modulus $E(\rho_i)$ of element i is scaled by the associated density ρ_i raised to the power p:

$$E(\rho_i) = \rho_i^p E_0, \tag{2}$$

where E_0 is the prescribed Young's modulus. The element stiffness matrix $\boldsymbol{K}_i$ is calculated based on the penalized modulus $E(\rho_i)$, and then assembled to the global stiffness matrix $\boldsymbol{K}$, defined as:

$$\boldsymbol{K}(\boldsymbol{\rho}) = \sum_{i=1}^{n} \boldsymbol{K}_i. \tag{3}$$

The gradient-based Method of Moving Asymptotes (MMA) [55] is used to update the densities in every optimization iteration. The design sensitivities of the structural compliance $C(\rho_i)$ and volume constraint $V(\rho_i)$ are required. The sensitivity of the volume constraint $\partial V/\partial\rho_i$ simply equals the volume of the i-th element V_i. Following the adjoint method, the sensitivity of the compliance is given by:

$$\frac{\partial C}{\partial \rho_i} = -\boldsymbol{U}^{\mathrm{T}} \frac{\partial \boldsymbol{K}}{\partial \rho_i} \boldsymbol{U}. \tag{4}$$

Based on the element-wise assembly of global stiffness matrix $\boldsymbol{K}$ (Eq. (3)) and given the SIMP material interpolation (Eq. (2)), this simplifies to the following expression on element level:

$$\frac{\partial C}{\partial \rho_i} = -p(\rho_i)^{(p-1)} \boldsymbol{U}_i^{\mathrm{T}} \boldsymbol{K}_0 \boldsymbol{U}_i, \tag{5}$$

where, $\boldsymbol{U}_i$ is the element nodal displacement vector, and $\boldsymbol{K}_0$ is the original element stiffness matrix of a fully solid element.

In order to avoid mesh dependence and checker-board problems [53] in the optimization process, a density filter is adopted. The densities are filtered as:

$$\bar{\rho}_i = \frac{\sum_{j=1}^{n} h(i,j)\rho_j}{\sum_{j=1}^{n} h(i,j)}. \tag{6}$$

Here, h is the convolution kernel defined as:

$$h(i,j) = \max(0, r_0 - r(i,j)), \tag{7}$$

where r_0 is a specific radius and $r(i,j)$ indicates the centroid distance between the element i and the element j. Based on the filtered densities $\bar{\rho}$, the chain rule is used to obtain consistent sensitivities. The optimization process terminates when the relative compliance

difference between two subsequent iterations is less than a given threshold (0.1% in this paper) and the volume constraint is satisfied.

Based on the design problem in Fig. 1, a FEM model with 180×60 elements is generated. Concrete material properties are adopted of which the Young's modulus is 30 GPa and the Poisson ratio is 0.15. In the TO process, the density power is $p = 3$, the volume constraint is taken as $\alpha = 25\%$and the filter radius is $r_0 = 1.5 \times$ (meshsize). After 103 TO optimization iterations, the optimized topology of this example is obtained, as shown in Fig. 3.

Fig. 3. Optimized topology of the dapped-end beam. Black and grey pixels indicate the solid and void regions.

2.2. Topology extraction phase

The purpose of this phase is to extract a truss-like structure from the obtained TO, as the next step towards an OPT-STM model. There have been several studies on extracting designs from TO results for different purposes, which we briefly review here. Lin and Chao [43] used several shape templates to represent holes in the TO results. Hsu and Hsu [33] adopted B-splines to describe the boundaries of TO results. Chou and Lin [20] and Yi and Kim [60] identified the geometrical features of TO results, and proceeded with shape and size optimization-based on the obtained features. Cuillière et al. [22] and Yin et al. [61] extracted 3D TO results to CAD-friendly models for the further utilization. However none of these methods was dedicated to extract STM models from the TO results. In this section, an automatic extraction method is proposed, which is specifically conceived to extract truss-like models from continuum TO results for the STM method. The method is a refinement of the method we have presented in an earlier study [59], and in particular the robustness of the connectivity identification is improved.

The proposed extraction method contains three steps (Fig. 2): (1) transforming TO results to binary data; (2) Thinning TO results into image skeletons; (3) Identifying nodes and their connections for the generation of truss-like structures. These three steps are described in more detail below.

1. Transforming TO results to binary data. Although TO results largely denote void/solid regions of structural domains, some of the densities have intermediate values. Clear binary data is required in Step 2, thus TO results are transformed to binary data by setting a threshold. In order to maintain the original topology in the binary data, in this paper the threshold is set to 0.1. All densities below this value are converted to the void state, and the remainder is set to solid. The binary image generated from the optimized topology (Fig. 3) is shown in Fig. 4.

2. Thinning TO results for skeletons. In order to extract truss-like structures effectively, optimized topologies are simplified through the thinning process introduced by Zhang and Suen [67]. The binary images are skeletonized by iteratively removing boundary pixels until no further pixels can be removed without changing the topology. In the thinning process, pixel-wise elimination rules are applied to determine the boundary pixels which are removable without changing the topology. Next, based on elimination rules, every pixel is marked to remove or remain, depending on the values of its eight neighbour pixels. The whole binary image is

Fig. 4. The binary image based on the TO result.

thinned iteratively in this manner. For the detailed elimination rules and further discussion of this thinning process, the reader is referred to Zhang and Suen [67]. Moreover, in our study, the load and support points are taken as unremovable pixels in the thinning method, as these must remain in the final STM model. The obtained skeleton of the adopted example (Fig. 4) is shown in Fig. 5. Note that the topology is unchanged, and members are represented by single-pixel curves.

3. Identifying nodes and connections for the generation of truss-like structures. The STM model is a truss-analogy model consisting of a network of nodes and their connections. Moreover, this truss-analogy model uses the axial-equilibrium forces to indicate the assumed force flow of a structure. Based on the obtained skeleton from the previous step, the truss-like structure generation method proceeds by identifying nodes and their connections. The detailed extraction procedures are introduced below.

First, nodes are detected based on the binary skeleton. Since the obtained skeleton curve is at most a single pixel wide, node detection rules are defined to identify candidate nodes by checking every pixel in the skeleton. The node detection patterns are presented in Fig. 6. Note that Patterns 1–4 include four rotationally equivalent cases, as is shown for Pattern 1 only. Every pixel in the skeleton and its eight neighbouring pixels is probed, and if the pattern matches one of these sets, it is identified as a candidate node. Moreover, the load and support points are taken as candidate nodes as well. The candidate nodes of the example (Fig. 5) are presented in Fig. 7a in red. Based on the node detection pattern, several candidate nodes may cluster in a small region, and a reduction method is used to eliminate redundant candidate nodes. In this paper, if the distance between two candidate nodes is smaller than $1.5 \times$ the mesh size, they are replaced by a single node at the rounded-averaged location in the skeleton. The reduced set of candidate nodes exclusively contains the identified nodes and is shown in Fig. 7b.

After identifying the nodes, their connections are required for the generation of a truss-like structure. Since all detected nodes are attached to the one-pixel wide skeleton, a recursive method is proposed to generate node connections. The method node-wisely checks every identified node. By iteratively detecting the skeleton pixels from the eight neighbouring pixels, a path from the considered node to other nodes connected by the skeleton curve is determined. This path defines a connection between two

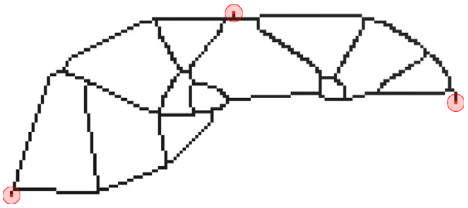

Fig. 5. The skeleton after the thinning process. The pixels marked in red circles are load and support points, and they are unremovable. (For interpretation of the references to color in this figure legend, the reader is referred to the web version of this article.)

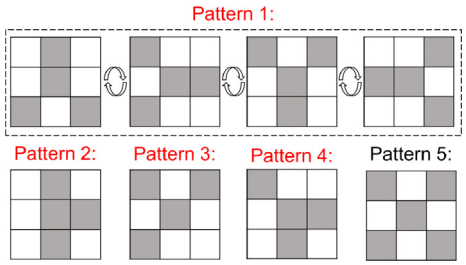

Fig. 6. Node detection patterns. Red patterns indicate that they have rotationally equivalent cases. (For interpretation of the references to color in this figure legend, the reader is referred to the web version of this article.)

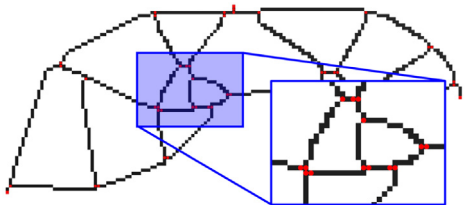

(a) Candidate nodes generated based on the skeleton, indicated in red

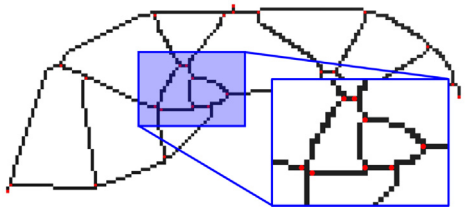

(b) Identified nodes by eliminating redundant nodes, indicated in red

Fig. 7. Node identification of the truss-like structure.

nodes, and is replaced by a bar in the truss-like structure. The generated truss-like structure of the example is presented in Fig. 8. Note that the curved lines in the skeleton are now replaced by straight bars, while maintaining the original topology.

The initially generated truss-like structure may have various short bars. These short bars, while structurally insignificant, are adverse for the generation of STM models. They increase the number of optimization variables in the subsequent shape optimization phase and can produce internal mechanisms in the truss model, which hamper in finding a static equilibrium state for the STM method. A merging method is proposed to eliminate these short bars. In the method, iteratively the lengths of all bars in the generated truss-like structure are checked. A typical situation is shown in the conceptual example in Fig. 9. Here the short bar B_i has two nodes, N_1 and N_2. In order to eliminate this short bar, a new node

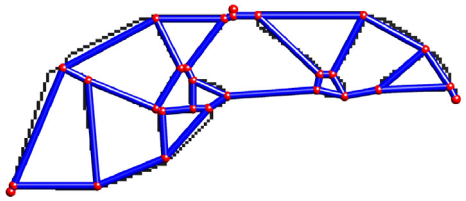

Fig. 8. The generated truss-like structure. Red points indicate the identified nodes and blue lines indicate their connections. (For interpretation of the references to color in this figure legend, the reader is referred to the web version of this article.)

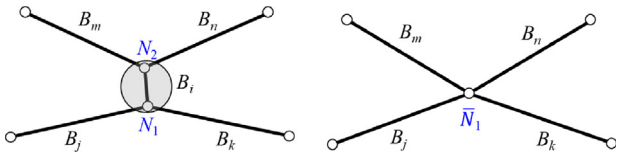

(a) Before merging (b) After merging

Fig. 9. The example of merging a short bar.

$\bar{N}_1$ is created replacing nodes N_1 and N_2 by their average. In the dapped-end beam example, considering a merging length $L_0 = 25.4$ mm (10% of the smallest outside dimension of the beam), the refined truss-like structure after removing 10 short bars is shown in Fig. 10. Note that the topology simplification leads to a structure that does not fully correspond to the TO result. A possible increase in compliance will however be counteracted in the final shape optimization phase.

2.3. Shape optimization phase

In most cases, the generated truss-like structures are statically and kinematically unstable structures, and their equilibrium forces cannot be calculated through truss analysis. In order to obtain equilibrium forces of the generated truss-like structures, instead of truss elements the classical beam element with a high slenderness (height/length = 0.001) is used. However, the obtained equilibrium forces cannot guarantee the generated truss-like structures can be used as STM models, because of the existence of shear forces. Based on the lower bound theory in the STM method, a pure axial force equilibrium state is required and shear forces should be zero. Thus, the generated truss-like structures can only be applied as STM models if a network of axial equilibrium forces is obtained. In this section, a shape optimization procedure is proposed to obtain an axial-force equilibrium while satisfying the geometry requirements. The generated truss-like structures are adjusted in the shape optimization process by modifying the internal node positions. After this process, a statically stable truss is obtained, referred to as the optimization-based Strut-and-Tie model (OPT-STM). The detailed steps are presented below.

2.3.1. Pure axial-force equilibrium requirement

In order to quantify the closeness of the generated truss-like structures to a pure axial force equilibrium state, the Suitable Truss Structure (STS) index has been proposed based on axial and shear forces obtained from beam analysis with slender beams and rigid joint connections [59], defined as:

$$\mathrm{STS} = \frac{1}{n}\sum_{e=1}^{n}\frac{|N_e|}{|N_e| + |V_e|}, \tag{8}$$

where, N_e is the element axial force, V_e is the element shear force, and n is the number of elements. The STS index has range $[0, 1]$. When STS $= 1$, all members in the truss-like structure are subjected to axial forces only and it can be used as-is in the STM method. The STS index of the illustrative example (Fig. 10) is 0.933.

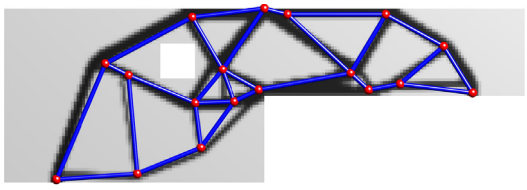

Fig. 10. The refined truss-like structure.

2.3.2. Including geometric requirements

Several geometric requirements that are important for practical application of the STM method are considered in this shape optimization process. Minimum required cover depths apply for the positions of the ties. Also the struts should have a minimum distance to the outer surface of the concrete element to ensure sufficient widths of these struts. This also applies to holes in the structure. These aspects were not taken into account in the TO phase, and the truss-like structure obtained after Step 2 may not be admissible.

A geometrical constraint is formulated to quantify these requirements, assuming rectangular impermissible areas. More complex regions can be represented by combinations of rectangles, a generalization to arbitrary shapes is left as a future extension. Two geometrical conditions are presented in Fig. (11), in which the grey areas denote the impermissible areas. In the first condition the bar, that is the line segment along the blue line, is crossing the rectangle, but its endpoints (nodes) are outside. In the second condition a bar crosses an edge of the rectangle, and one of its nodes lies in the impermissible region.

In the first case, bar-to-corner distance vectors are used to formulate a geometrical constraint for the shape optimization procedure. Constraint violation is measured by the perpendicular distance from the bar to the nearest corner of the impermissible region. As a result, during optimization the bar will move towards this corner and out of the rectangle. In Fig. 11a, $\boldsymbol{v}_i$ are five vectors from the four corners ($i = 1$ to 4) and the centre point ($i = 0$) of the impermissible area to an endpoint of the bar. The five vector distances $\boldsymbol{d}_i$ between the centre and corner points of the impermissible area and the bar vector $\boldsymbol{v}_*$ are calculated as:

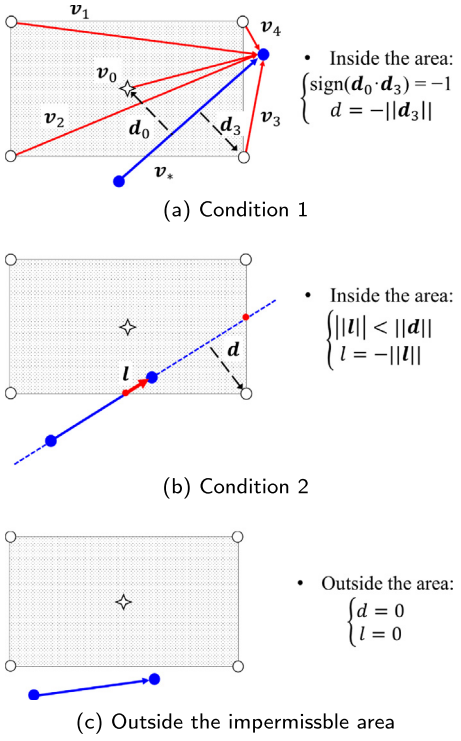

Fig. 11. Example illustrating the geometry constraint. Blue points indicate two nodes of a bar. Black circles and stars indicate the four corners and the centre point of a rectangular impermissible area respectively. Red points indicate the intersection points. (For interpretation of the references to color in this figure legend, the reader is referred to the web version of this article.)

$$\boldsymbol{d}_i = \left(\mathrm{I} - \frac{\boldsymbol{v}_* \otimes \boldsymbol{v}_*}{\|\boldsymbol{v}_*\|^2} \right) \boldsymbol{v}_i, \tag{9}$$

where I is the identity matrix and $\otimes$ denotes the dyadic tensor product. In this case, the geometrical constraint is defined by the scalar distance using d, defined as:

$$d = \sum_{i=1}^{4} \min[0, \text{sign}(\boldsymbol{d}_0 \cdot \boldsymbol{d}_i)] \|\boldsymbol{d}_i\|. \tag{10}$$

In this equation, $\text{sign}(\boldsymbol{d}_0 \cdot \boldsymbol{d}_i)$ is the sign operator applied on the inner product of distance vectors. If the bar passes the corner of the rectangle at the same side as it passes the centre point then $\text{sign}(\boldsymbol{d}_0 \cdot \boldsymbol{d}_i) = 1$, otherwise -1 is obtained. A negative d indicates that the bar is crossing the rectangle. If the bar lies outside the impermissible area then $d = 0$.

In the second case (a bar node that is within the impermissible area), next to the distance calculated from the first condition, the penetration length is considered to evaluate the constraint violation. The bar is thus steered to move out of the impermissible area along the bar direction. The intersecting line segment of the bar with the impermissible area is presented as $\boldsymbol{l}$ in Fig. 11b. Note that when the bar entirely falls inside the impermissible area, $\boldsymbol{l}$ equals the full bar length. The geometry constraint is given by the length l, defined as:

$$l = -1 \cdot \min(\|\boldsymbol{l}\|, |d|). \tag{11}$$

Combining the two conditions together, the geometry constraint g_m^n of the bar n with respect to the impermissible area m is calculated as:

$$g_m^n = \begin{cases} d & \text{Condition 1} \\ l & \text{Condition 2} \\ 0 & \text{Outside the area} \end{cases}. \tag{12}$$

Based on this constraint measure, g_m^n is zero when bar n and rectangle m do not overlap or intersect (Fig. 11c), and $g_m^n \leqslant 0$ otherwise. In the illustrative example, six impermissible regions are introduced to ensure sufficient cover and maintain the opening, as presented in Fig. 12.

2.3.3. The shape optimization problem

Based on the above aspects, and continuing with the same objective as used in Phase 1 (Eq. (1)), the mathematical formulation of the shape optimization problem is given by:

$$\begin{aligned} \text{minimize}: \quad & C(\boldsymbol{x}) = \boldsymbol{F}^{\mathrm{T}} \boldsymbol{U}(\boldsymbol{x}) \\ \text{subject to}: \quad & \boldsymbol{K}(\boldsymbol{x}) \boldsymbol{U} = \boldsymbol{F} \\ & \text{STS} \geqslant 1 - \varepsilon \\ & \sum_{j=1}^{n} g_m^j \geqslant 0 \quad (m = 1, 2 \ldots) \\ & \boldsymbol{x}_{\min} \leqslant \boldsymbol{x} \leqslant \boldsymbol{x}_{\max} \end{aligned} \tag{13}$$

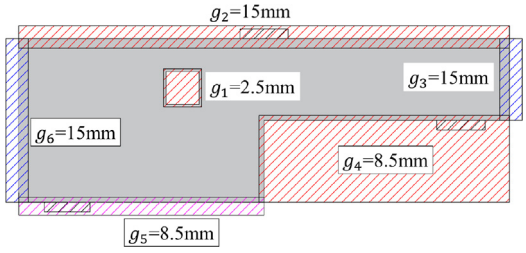

Fig. 12. The geometry constraint regions. Six rectangular regions defining the required cover layers and the opening are highlighted with dashed lines.

where $\boldsymbol{x}$ is a vector containing the coordinates of the nodes of the generated truss-like structure, which are used as optimization variables. $\boldsymbol{x}_{\min}$ and $\boldsymbol{x}_{\max}$ are the minimum and maximum coordinates of the structural domain. Furthermore, m is the index of an impermissible area and n is the number of bar elements. $C, \boldsymbol{F}, \boldsymbol{U}$ and $\boldsymbol{K}$ here represent the compliance, nodal forces, nodal displacements and the stiffness matrix based on the beam finite element model. STS is the axial force equilibrium indicator introduced in Eq. (8). Note that in this shape optimization, a tolerance ε is allowed. Bending moments and shear forces are inevitable when using beam elements. Therefore, ε is taken as 0.005 in this study in order to obtain nearly purely axial equilibrium forces. The inequality $\sum_{j=1}^{n} g_m^j \geqslant 0$ is the constraint with respect to region m to guarantee geometry requirements. Summing all constraints per region into a single inequality reduces the computational costs in the optimizer due to a large number of optimization constraints.

Similar to the TO phase, the MMA optimization algorithm is used to solve this problem. Central finite differences are used to calculate sensitivities. The perturbation is taken as a value at 0.1% of the mesh size of the continuum elements. The problem defined by Eq. (13) is a nonconvex constrained optimization problem. In order to ensure robust convergence, a move limit of 10% of the mesh size of the continuum elements is imposed on the design variables.

The result after shape optimization of the example problem is shown in Fig. 13, and the difference compared to the previous model is shown in Fig. 14. The convergence history of the objective value and constraints (g_2, g_4 and g_5 regions are shown in Fig. 12) is presented in Fig. 15. Some oscillation in constraint g_4 is observed which is due to the non-smoothness of the geometrical constraints, but the applied move limit is effective in stabilizing the optimization process. Although small node position differences are observed in Fig. 14, the suitability for the STM method is improved significantly in this final shape optimization step. After 70 optimization iterations, the compliance converges after a considerable improvement, and the STS index has increased from 0.933 to 0.9997 while the geometry constraints g_2, g_4 and g_5 are reduced to 0 mm. g_1, g_3 and g_6 remained zero for all iterations. This indicates that a near ideal axial force configuration has been obtained, that also meets all geometrical requirements. With all three phases combined, the automated generation process took about 4 min for the considered example. The generated OPT-STM is shown in Fig. 16 which can be used for STM analysis.

2.3.4. STM analysis

To complete the process, an STM analysis is conducted for the generated OPT-STM based on the European code [17] while disregarding partial safety factors. The average concrete compressive strength is 62.8 MPa (from the experiment by Oviedo et al. [47]). The limit strength of struts and node zones is defined as:

$$\sigma_{\max} = k\nu f_{\mathrm{cm}}, \tag{14}$$

where f_{cm} is the concrete compressive strength and ν is the concrete effectiveness factor determined as, with f_{cm} in MPa:

$$\nu = 1 - f_{\mathrm{cm}}/250. \tag{15}$$

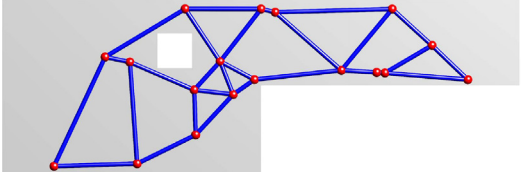

Fig. 13. The generated truss-analogy model after the shape optimization phase.

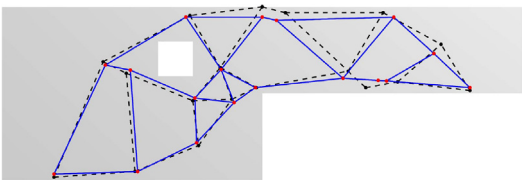

Fig. 14. Comparison of two models. The blue solid lines present the model after shape optimization, while the black dashed lines present the truss obtained after Step 2. (For interpretation of the references to color in this figure legend, the reader is referred to the web version of this article.)

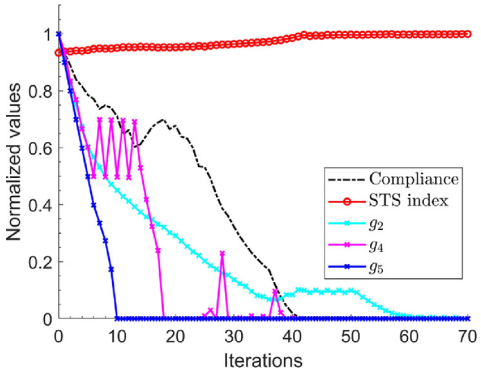

Fig. 15. Shape optimization convergence history.

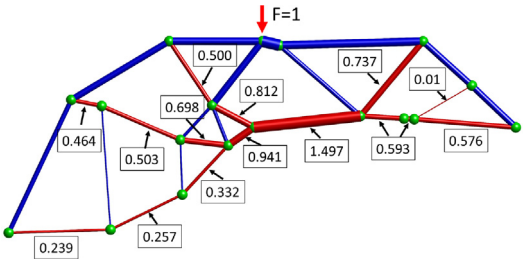

Fig. 16. The generated OPT-STM. The blue and red lines indicate struts and ties respectively. The line width indicates the magnitude of axial forces. Normalized tensile forces (for a unit loading) are presented. (For interpretation of the references to color in this figure legend, the reader is referred to the web version of this article.)

In Eq. (14), k is a reduction factor which is 1 or 0.85 for the concrete compressive strength of the C-C-C nodes (nodal zones bounded by three or more struts) and C-C-T nodes (nodal zones bounded by two or more struts and a tie) respectively. All nodal zones with large compressive forces are checked, as illustrated in Fig. 17. In the strength checking of struts, $k = 0.6$ for the strut with transverse tension is used, otherwise $k = 1$. Based on the given dimensioning, a summary of the strut checking results is given in Table 1. The generated OPT-STM satisfies the STM stress requirements.

For the ties, it is assumed that all reinforcements in the STM designs are fully activated. The reinforcement cross-sectional areas are determined based on a 100% strength utilization and omitting partial safety factors.

3. Strut-and-Tie model evaluation method

The intuition of engineers alone is not effective for evaluating the performance and capacities of complex STM models. In order to investigate the suitability of the generated OPT-STMs, an evaluation method based on Nonlinear Finite Element Analysis (NLFEA)

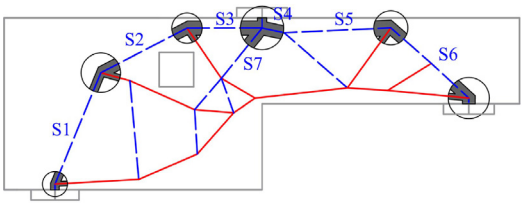

Fig. 17. Node regions of the generated OPT-STM model after STM analysis.

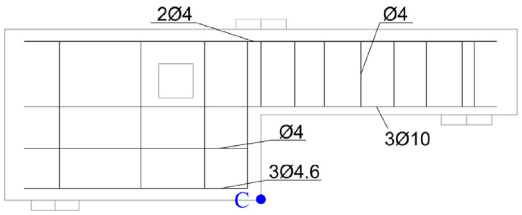

Fig. 18. Reinforcement layout of specimen A in Oviedo et al. [47] (mm).

Table 1
Summary of strut geometry and forces for STM.

Strut	Force (kN)	k	Width (mm)	Strength utilization (%)
S1	39.9	0.6	13	91
S2	57.5	0.6	18	94
S3	69.2	0.6	21	97
S4	108.7	1.0	20	96
S5	75.9	0.6	23	97
S6	56.8	0.6	18	93
S7	59.7	0.6	18	98

is proposed in this section. Nonlinear phenomena such as concrete cracking and crushing and steel yielding and rupturing are considered in the NLFEA. Firstly, simulating RC structures by NLFEA is validated with experimental data, as presented in the following section. Next, the NLFEAs based on the STM models are used to obtain the structural performance. The structural responses are compared in terms of crack distribution, failure load and failure mode to evaluate various STM models. Note that this NLFEA procedure is included here to investigate and demonstrate the performance of the OPT-STM model generated by the proposed method, instead of being part of that method.

3.1. Nonlinear finite element analysis of RC structures

The NLFEA has been broadly applied in simulating RC structures, and several guidelines have been produced to select suitable solution strategies, see e.g. in fib [26] and Belletti et al. [8]. In this section, to validate the simulation an experiment conducted by Oviedo et al. [47] is simulated by NLFEA. The considered specimen is based on the same dapped-end beam of the previous section (see Fig. 1), and its reinforcement layout in the experiment is shown in Fig. 18. The steel has been placed horizontally and vertically, reflecting a conventional RC structure.

In order to conduct the NLFEA simulation, various aspects are considered, such as material models, finite element discretization, iteration scheme and convergence criteria. According to the solution strategy by Belletti et al. [8] and based on the compressive strength 62.8 MPa obtained from the 28-day cylinder test in the experiment, the derived concrete properties are summarized in Table 2. The properties of steel reinforcements from the experiment are presented in Table 3. The steel stiffness, E_s, is 200 GPa. They are simulated by fully-bonded embedded truss elements connected to the concrete continuum elements. The other analysis choices are presented in Table 4.

The analysis model is shown in Fig. 19. The load and support plates are simulated using a linear material model with stiffness E_s and Poisson ratio 0.3, and interface elements are inserted between the steel plate and the concrete. The load-displacement curves of this simulation and the experimental result by Oviedo et al. [47] are presented in Fig. 20. The displacement is measured vertically at the middle-bottom point of the beam (C point in Fig. 18). The peak load of the simulation and experimental results

Table 2
Concrete properties

Mean compressive strength:	$f_{cm} = 62.8$ MPa
Mean tensile strength:	$f_{ct} = 4.21$ MPa
Fracture energy:	$G_F = 0.154$ N/mm
Compressive fracture energy:	$G_C = 38.45$ N/mm
Young's modulus:	$E_c = 39666$ MPa
Poisson ratio:	$v = 0.15$

Table 3
Reinforcement properties.

Diameter (mm)	Yield stress (MPa)	Ultimate stress (MPa)	Ultimate strain (%)
4	522	604	10
4.6	508	603	15
10	625	650	11.5

Table 4
NLFEA solution strategies [8].

– Finite element discretization:	8-node plane stress elements for concrete Embedded truss elements for reinforcement Mesh size: 7.5 mm
– Constitutive relation:	**Concrete**: • Rotating smeared crack model • Hordijk model for tensile behavior • Parabolic model for compressive behavior (reduction model by Vecchio and Collins [57], 0.6) **Reinforcement**: •Bi-linear strain-stress relation •Perfect bonded with concrete [25]
– Convergence criteria:	Displacement norm: 0.01 Force norm: 0.01
– Loading scheme:	Displacement control (Step size: 0.05 mm)

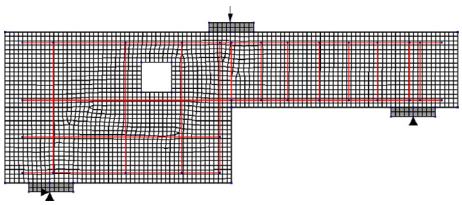

Fig. 19. Finite element model of the experimentally tested dapped-end beam.

are 119.0 kN (Point A in the curve) and 117.7 kN respectively. In the ultimate state (Point B), the structure fails due to steel rupturing. The strain in the steel and the rupturing location are presented in Fig. 21, and the crack patterns predicted by the simulation are shown in Fig. 22. The crack development of the simulation matches the observation in the experiment [47]. While cracking patterns, ultimate capacity and failure mode show good agreement with the experimental findings, the numerical analysis shows substantially smaller deformations than the experiments (Fig. 20). This

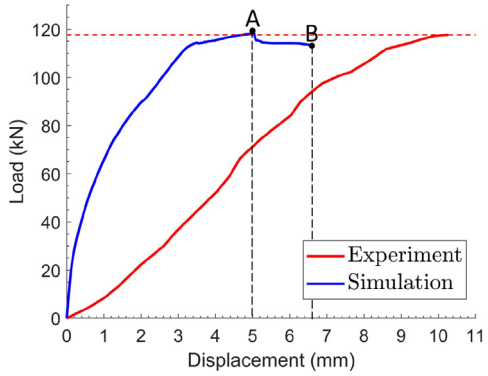

Fig. 20. Load-displacement curves of the experimentally tested dapped-end beam.

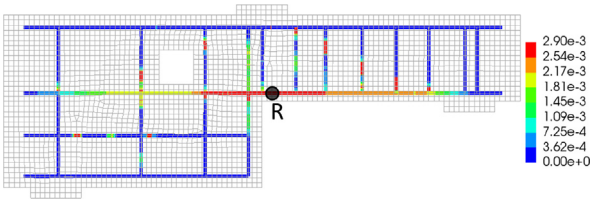

Fig. 21. Steel strain distribution at the ultimate state B (Point R indicates the rupturing location).

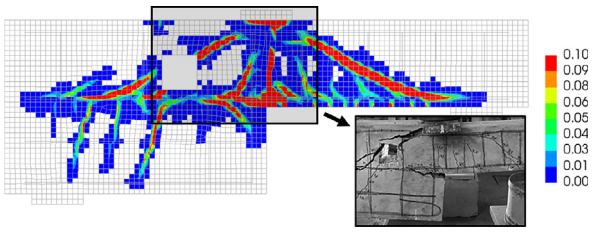

Fig. 22. Simulated and experimental (inset) crack patterns and widths (mm) at the ultimate state B of the experimentally tested dapped-end beam. The inset is adapted from Oviedo et al. [47].

can be attributed to a too high estimate of the Young's modulus in the analysis, inadequate modelling of the stiffness of the support and loading systems, which possibly included felt or plywood layers, or deformations within the loading frame. It is likely that these aspects only influence the prediction of the deformation capacity. Considering the lack of experimental data on these aspects, and the fact that the main use of the NLFEA is to predict the loading capacity and failure mode, no further efforts are considered to improve the displacement predictions. The current solution strategy is used to evaluate Strut-and-Tie models.

3.2. NLFEA-based evaluation method of Strut-and-Tie models

In order to evaluate the performance of complex STM models, NLFEA is used. It is assumed that reinforcement bars are located corresponding to the ties in the STM model. In this way, practical reinforcement detailing aspects are excluded from the procedure and all NLFEAs are based on the same principle and the obtained responses can be used for comparing various STM models. The cross sections of these bars are based on full utilization of the yielding stress at the design load. The yield strength of steel is set to 580 MPa, without hardening effects and applying a rupturing strain of 10%.

Based on the obtained forces of the OPT-STM from the illustrative example (Fig. 16), the resulting finite element model is shown in Fig. 23. The total steel volume is 87452 mm^3. In the NLFEA, the same solution strategies as in the previous section are used to calculate structural responses. The obtained load-displacement curve through the NLFEA is presented in Fig. 24. The ultimate capacity reaches 81.7 kN while the design load for the STM analysis is 71.2 kN. The crack pattern and steel strain at the ultimate state (Point A) are shown in Fig. 25. Most reinforcements are yielding, and the structure collapses due to steel rupturing at the ultimate state and results in a flexural failure mode.

The evaluation process demonstrated here on this OPT-STM model is used in the later sections to evaluate various other STM models. We also define a dimensionless ratio that expresses the degree of utilization of the steel reinforcement for later comparisons. This ratio, named *PV* ratio, is given by:

$$PV = \frac{P_{\text{load}} L_k}{V f_y}, \tag{16}$$

where P_{load} is the peak load obtained from the NLFEA, V is the total steel volume, f_y is the steel yield strength and L_k is a characteristic length of the structure. In this paper, L_k is taken as the smallest height of the structure. In the presented OPT-STM example, L_k equals to 127 mm and the resulting *PV* ratio is 0.205. Before using the measures introduced in this section for a comparative evaluation of OPT-STM designs against classical STM models, they are applied in the next section to study several aspects of the proposed generation process.

4. Three aspects of the automated design method for OPT-STM models

In this section, three main aspects influencing the generation of OPT-STM models are discussed. Different settings and parameters in the generation method will affect generated OPT-STM models. Firstly, in the TO phase (Section 2.1), TO is conducted to generate optimized material distributions. The volume fraction and filter radius affect the optimized topology and thus influence the generated OPT-STM models. The influence of these two factors will be demonstrated and discussed. Next, in the topology extraction phase (Section 2.2), the merging of short bars (Fig. 9) simplifies the extracted truss-like structures. However, by adopting different merging lengths the generated OPT-STM models are affected. The influence of the merging length will be demonstrated and discussed. Thirdly, regarding the STM generation phase, the importance of satisfying the axial force equilibrium is discussed.

4.1. Influence of volume fraction and filter radius in the topology optimization phase

The volume fraction (α) affects the number of members and their width in the topology results. The topological changes will influence the generated OPT-STM models and their performance. Next to the volume fraction, the filter radius (r_0) smoothens the TO results to prevent mesh dependency and checker-board prob-

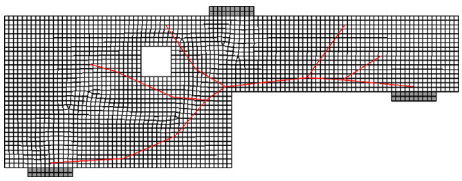

Fig. 23. Finite element model based on the generated OPT-STM for the dapped-end beam.

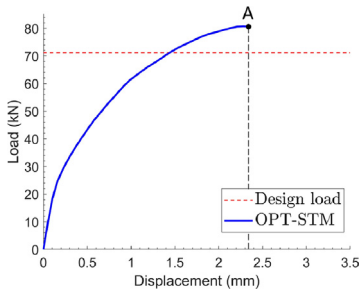

Fig. 24. Load-displacement curve of the OPT-STM based design.

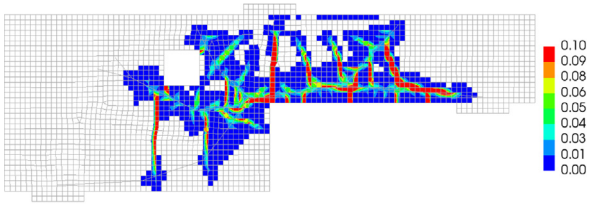

(a) Simulated crack patterns and widths (mm) at the ultimate state A

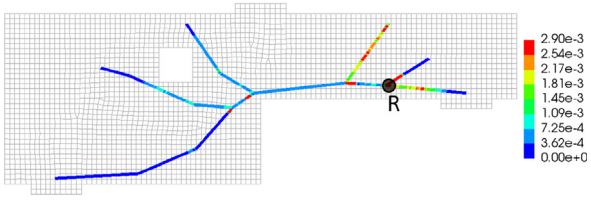

(b) Steel strain distribution (Point R indicates the rupturing location)

Fig. 25. NLFEA simulation results of the OPT-STM based design.

lems in the TO process. With a large filter radius, a TO result with fewer members is obtained. In order to investigate the influence of these parameters, OPT-STM models of the illustrative example with various volume fractions and filter radii are generated, and their performance is evaluated using both the *PV* ratio and the load-displacement curve obtained through NLFEA.

In the illustrative example, the OPT-STM model is generated with volume fraction $\alpha = 25\%$ and filter radius $r_0 = 1.5$. Here, four other OPT-STM models are generated based on a one-factor-at-a-time sensitivity analysis. In these four models the volume fraction is $\alpha = 15\%$ and $\alpha = 35\%$ and the radius is $r_0 = 2.5$ and $r_0 = 3.5$ respectively. The topology optimization results and the resulting OPT-STM models are shown in Fig. 26. All OPT-STM models have STS indices larger than 0.995 and satisfy the geometry constraints. The evaluation results based on the proposed evaluation method are presented in Table 5. The load-displacement curves are presented in Fig. 27.

Based on the calculated *PV* ratios of changing volume fractions ((Fig. 26 (a), (b) and (c))), we observe that the OPT-STM model with $\alpha = 15\%$ performs better than the other two cases regarding the ultimate capacity and steel usage. The variations of OPT-STM models for a changing filter radius are presented in Fig. 26 (b), (d) and (e). The OPT-STM model performs better with a relatively small radius ($r_0 = 1.5$). NLFEA shows that all designs based on these OPT-STM models provide higher capacities than the design load, as seen in Fig. 27. This observation confirms that STM results in conservative designs. Although different material distributions are obtained in the TO results, all models show similar load-displacement curves and the resulting structures fail due to steel

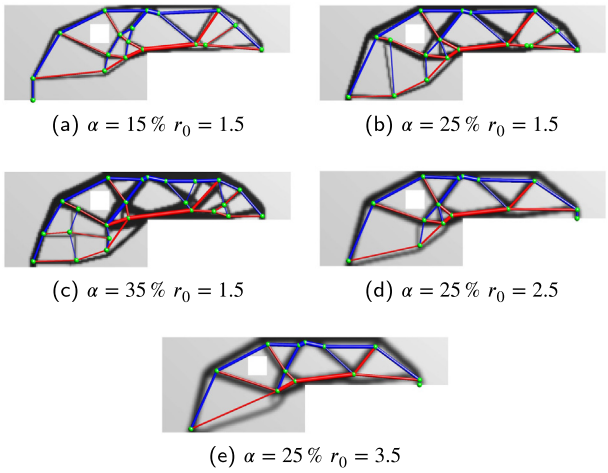

(a) $\alpha = 15\,\%$ $r_0 = 1.5$ (b) $\alpha = 25\,\%$ $r_0 = 1.5$

(c) $\alpha = 35\,\%$ $r_0 = 1.5$ (d) $\alpha = 25\,\%$ $r_0 = 2.5$

(e) $\alpha = 25\,\%$ $r_0 = 3.5$

Fig. 26. The generated OPT-STMs with different parameters. Black pixels present the TO result. The blue and red lines indicate struts and ties respectively. The line width indicates the magnitude of axial forces. (For interpretation of the references to color in this figure legend, the reader is referred to the web version of this article.)

Table 5
Peak load, steel volume and *PV* ratio of evaluated OPT-STM models.

α (%)	r_0 (mesh size)	Peak load (kN)	Steel volume (mm^3)	*PV* (%)
15	1.5	82.10	**86630**	**20.9**
25	1.5	81.73	87452	20.5
35	1.5	79.08	92693	18.2
25	2.5	**84.17**	91116	20.2
25	3.5	82.95	92927	19.5

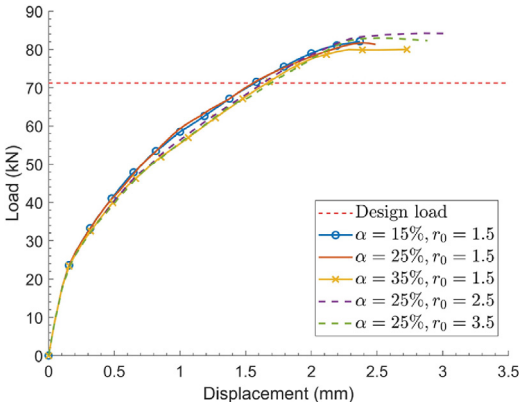

Fig. 27. Load-displacement curves of evaluated OPT-STM models.

rupturing. However, the models with a relatively large volume fraction and filter radius have lower *PV* ratios. Moreover, from results not shown in this paper, it has been found that adopting even larger volume fractions ($\alpha = 50\%$) or larger filter radii ($r_0 = 6$) leads to unclear topologies, which do not allow generation of truss-like structures and the OPT-STM models. Therefore, a relatively small volume fraction and filter radius are suggested in the TO phase.

4.2. Influence of merging length in the topology extraction phase

The merging length L_m is used to eliminate short bars in the topology extraction phase. This simplification will influence the

accuracy of extracted truss-like structures in representing TO results and thus influence the performance of the resulting OPT-STM models. The merging length L_m is taken as: r_L times the smallest outside dimension of the illustrative example. A fraction $r_L = 10\%$ results in a merging length of 25.4 mm for the considered beam example. The corresponding reference result is shown in Fig. 26b. In this section, in order to investigate this parameter, two more OPT-STM models are generated with fractions $r_L = 15\%$ and $r_L = 25\%$ respectively. The generated OPT-STM models are presented in Fig. 28.

The obtained results for these models are shown in Table 6. The complexity of the OPT-STM models is reduced with increasing merging lengths. Regarding the evaluation results of $r_L = 10\%$ and $r_L = 15\%$, we observe similar *PV* ratios. By reducing the merging length, a more accurate and detailed truss-like structure is obtained in the topology extraction phase, and the resulting OPT-STM has a higher *PV* ratio. The OPT-STM generated with $r_L = 25\%$ has an obviously different truss analogy model than the other two cases. In this case, the structure fails due to steel rupturing, as shown in Fig. 29. The limited steel ductility and concrete plasticity are not able to re-distribute stresses to fully utilize the steel, therefore the ultimate capacity is lower than the design load (71.2 kN).

These findings confirm that the merging length affects the extracted truss-like structures. Although large merging lengths reduce the complexity of OPT-STM models, the generated models are no longer representative of the TO results, and a poor performance is obtained which has a lower capacity, a higher steel usage and a lower *PV* ratio. By choosing suitable lengths, the generated OPT-STM models are effective in representing the TO results and have good performance.

4.3. Importance of satisfying the axial force equilibrium

Axial force equilibrium states of truss-analogy models are required in the STM method. The designs based on the STM method are conservative which is an important aspect in practice. The extracted truss-like structures are usually statically and kinematically unstable structures in which the calculated STS indices (Eq. (8)) are substantially smaller than 1. Through shape optimization, the final OPT-STM structure closely approximates a pure axial force system. In order to investigate the importance of this shape optimization step and of satisfying the axial force equilibrium, the extracted uncorrected truss-like model excluding the shape optimization phase is analyzed, as shown in Fig. 10. The STS index

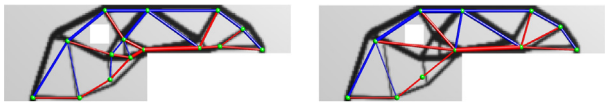

Fig. 28. Generated OPT-STMs with two merging lengths. Black pixels present the TO result. The blue and red lines indicate struts and ties respectively. The line width indicates the magnitude of axial forces. (For interpretation of the references to color in this figure legend, the reader is referred to the web version of this article.)

Table 6
Peak load, steel volume and *PV* ratio of evaluated OPT-STM models.

r_L (%)	Peak load (kN)	Steel volume (mm^3)	*PV* (%)
10	**81.73**	87452	**20.5**
15	79.45	**85799**	20.3
25	65.89	88929	16.2

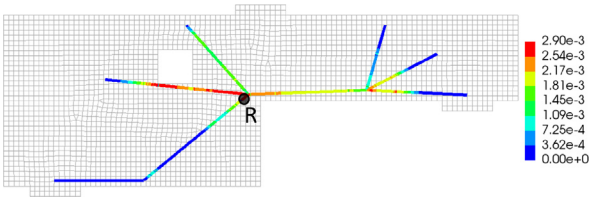

Fig. 29. Steel strain distribution of the model ($r_L = 25\%$) (Point R indicates the rupturing location).

of this truss-like structure is 93.3%. After the beam analysis, only axial forces are used to design cross sections of the reinforcement in the NLFEA model. The evaluation results are summarized in Table 7, and load-displacement curves are presented in Fig. 30.

The evaluation result of the uncorrected truss-like structure shows a capacity significantly below the design load, which is supposed to be a lower bound. The shear force diagram of the truss-like structure is presented in Fig. 31, and the crack patterns and the steel strain in the ultimate state are presented in Fig. 32. Due to the large shear forces, the structure fails in a shear failure mode without steel rupturing. The satisfaction of the STS index requirement is important to guarantee that the generated models are suitable for the STM method, and lead to safe designs.

5. Applications of the generation method for two D-regions

In this section, the generated OPT-STM models and 11 manually generated STM models from literature for two D-regions are evaluated. The first case (Case A) is the dapped-end beam which has already been used as illustrative example throughout the previous sections. The second case (Case B) is an irregular deep beam with an opening. Based on NLFEA results of these STM models, the load capacity, steel usage, *PV* ratios and failure modes are compared to evaluate the relative effectiveness of the generated OPT-STM models.

5.1. Problem description and Strut-and-Tie models

Case A was introduced in Fig. 1 in Section 2. Case B is based on Example Problem 4 of ACI SP-208 [50]. The experimental investiga-

Table 7
Peak load, steel volume and *PV* ratio of evaluated models.

Cases	STS index (%)	Peak load (kN)	Steel volume (mm^3)	*PV* (%)
Truss-like structure	93.3	43.98	78029	12.4
OPT-STM	99.97	81.73	87452	20.5

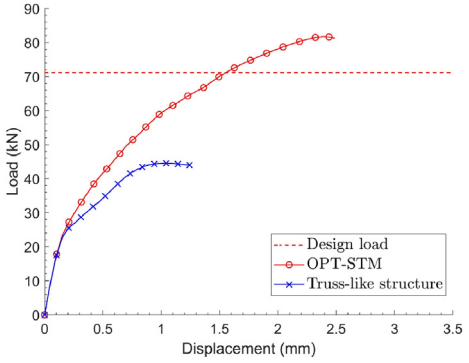

Fig. 30. Load-displacement curves of the OPT-STM and the uncorrected truss-like model.

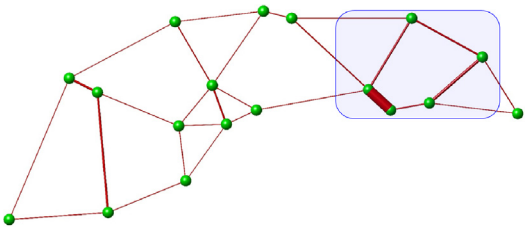

Fig. 31. The shear force diagram of the uncorrected truss-like structure. The bar width indicates the magnitude of shear forces.

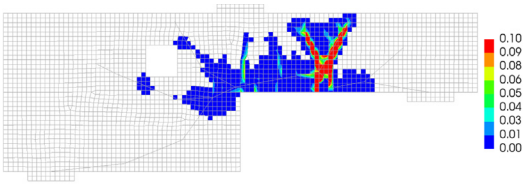

(a) Simulated crack patterns and widths (mm)

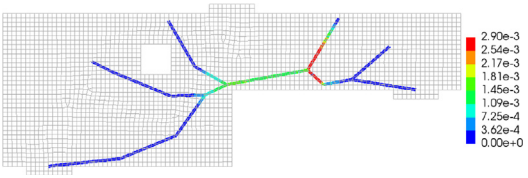

(b) Steel strain distribution

Fig. 32. Structural response of the uncorrected truss-like structure in the ultimate state.

tion of this problem was conducted by Ley et al. [41]. The geometry and loading conditions are presented in Fig. 33. The thickness of this structure is 38 mm.

Following the proposed generation method, and using the recommended settings obtained in Section 4 (volume fraction $\alpha = 25\%$, filter radius $r_0 = 1.5$, merging length $r_L = 10\%$), the OPT-STM model for this irregular deep beam is generated, as shown in Fig. 34. It has an STS index equal to 0.999, and is presented in Fig. 35.

The evaluated STM models of Case A from previous studies in literature are presented in Fig. 36. The OPT-STM model for this case is the same model as obtained in Section 2, Fig. 16. Four additional STM models from previous studies, as shown in Fig. 36(b)-(e) with corresponding references, are also evaluated. STM-A1, STM-A2 and STM-A3 have a similar right-hand side part, however the force transmission in the left-hand side part differs between these models. Model STM-A4 has been generated based on a topology optimization result with manual adjustments.

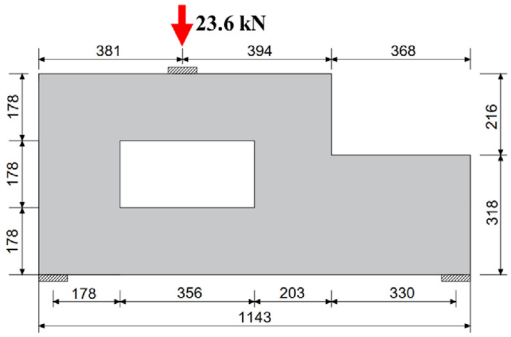

Fig. 33. Irregular deep beam with an opening (mm).

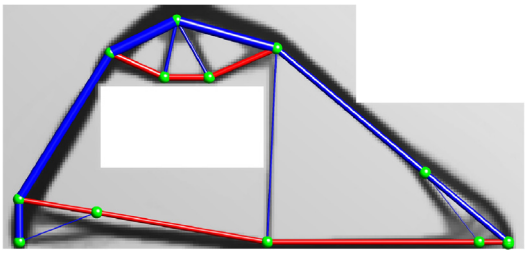

Fig. 34. The generated OPT-STM of the irregular deep beam.

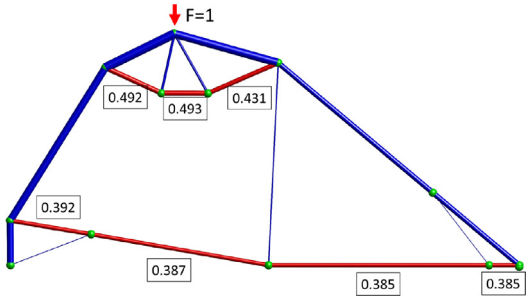

Fig. 35. The generated OPT-STM of the irregular deep beam. The blue and red lines indicate struts and ties respectively. The line width indicates the magnitude of axial forces. Normalized tensile forces (for an unit loading) are presented. (For interpretation of the references to color in this figure legend, the reader is referred to the web version of this article.)

As for Case B, seven previously proposed STM models are evaluated and compared against the generated OPT-STM model, as shown in Fig. 37. In this example, STM-B1 simulates two beams which are placed in the upper and lower part of the structure. STM-B2 simulates the force transmission as a portal frame with a hinge at the top. STM-B3 was proposed following the load path method. Compared to STM-B1, STM-B4 uses a deeper truss at the right-hand side. The motivation of the proposed STM-B5 is to provide a large amount of ductility. The stresses in the bottom part of the beam are neglected. STM-B6 and STM-B7 are created based on

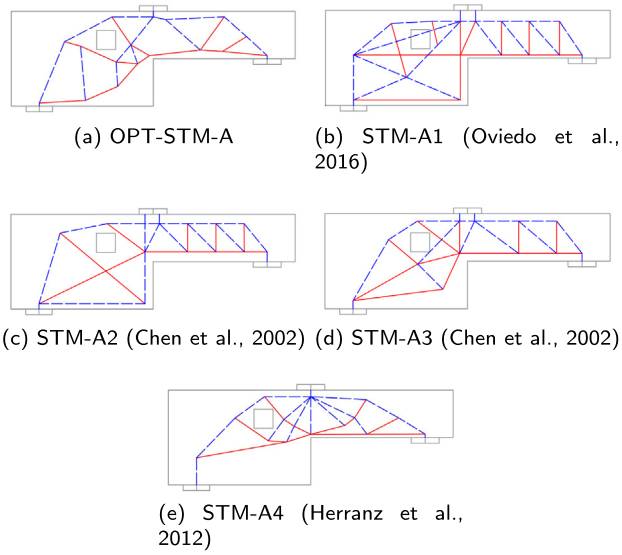

(a) OPT-STM-A (b) STM-A1 (Oviedo et al., 2016)

(c) STM-A2 (Chen et al., 2002) (d) STM-A3 (Chen et al., 2002)

(e) STM-A4 (Herranz et al., 2012)

Fig. 36. STM models for Case A (the dapped-end beam).

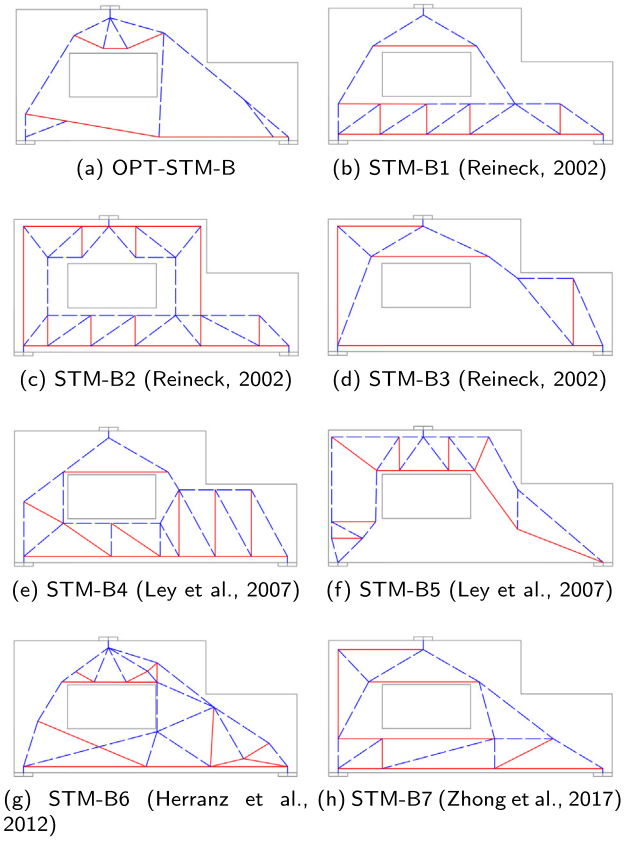

Fig. 37. STM models for Case B (irregular deep beam).

TO results, followed by manual interpretation. However, a large difference is observed between the TO result reported in Zhong et al. [68] and the resulting STM-B7.

5.2. Evaluation results and discussions

Based on the evaluation method from Section 3, the aforementioned STM models are evaluated by NLFEA. The solution strategy for Case A is the same as in the illustrative example. In Case B, the concrete properties are calculated based on a mean compressive strength as 21.4 MPa from the experiment by Ley et al. [41]. The step size is 0.01 mm in displacement control and the mesh size for the FEM model is 12 mm. Other aspects of the solution strategy remain the same as in the first example. All axial equilibrium forces of evaluated STM models are calculated based on the design load to determine cross-sectional areas for the reinforcements. The STS indices for the classical STM models approach 1, indicating pure axial loading. Given the high STS indices for both OPT-STM models, there is no difference between all models in this respect.

The obtained load-displacement curves of Case A are shown in Fig. 38. The ultimate load and steel usage are summarized in Table 8. The models with best and worst *PV* ratios have line markers in the load-displacement curves. In this example, all models fail due to steel rupturing and they have a peak load larger than the design load (71.2 kN). Moreover, the load-displacement curve shows that the OPT-STM model is generally stiffer than other models. It has the largest *PV* ratio which indicates the most economical design. STM-A2 has the lowest *PV* ratio, indicating a relatively costly design. Since STM-A4 was inspired by a TO result, a relatively large *PV* ratio is obtained compared to the other classical STM models. The proposed automated STM model generation process is superior to this hand-tuned model in both capacity and *PV*

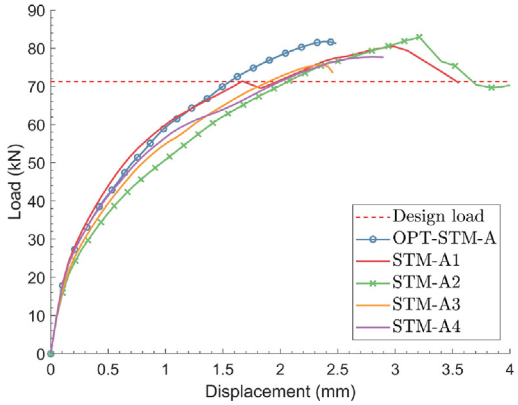

Fig. 38. The load-displacement curves for the STM models of Case A (dapped-end beam).

Table 8
The ultimate load and steel usage of STM models of the Case A (dapped-end beam).

Cases	Peak load (kN)	Steel volume (mm^3)	*PV* (%)
OPT-STM	81.73	87452	**20.5**
STM-A1	80.50	134202	13.1
STM-A2	82.91	189422	**9.6**
STM-A3	80.58	105979	16.6
STM-A4	77.72	84781	20.0

ratio, however in terms of absolute reinforcement volume the STM-A4 model has a slight advantage. Moreover, the peak loads of all models are reached when the reinforcement reaches the ultimate strain.

In Case B (irregular deep beam), the load-displacement curves of all evaluated models are presented in Fig. 39. The ultimate load and steel usage are summarized in Table 9. Similar as in the first example, the OPT-STM has the best *PV* ratio. STM-B6 is inspired by a TO result and also leads to a relatively good *PV* ratio. Because of the large differences between STM-B7 and its TO result, a lower *PV* ratio is obtained for STM-B7.

In this example, the peak loads of other models are considerably larger than the design load (23.6 kN) apart from STM-B5. The design of STM-B5 shows a brittle behaviour in which the reinforcement cannot be fully activated due to the limited plasticity of concrete. In this case, most STM models (except STM-B2 and STM-B5) fail due to steel rupturing. Because of stress redistribution, the

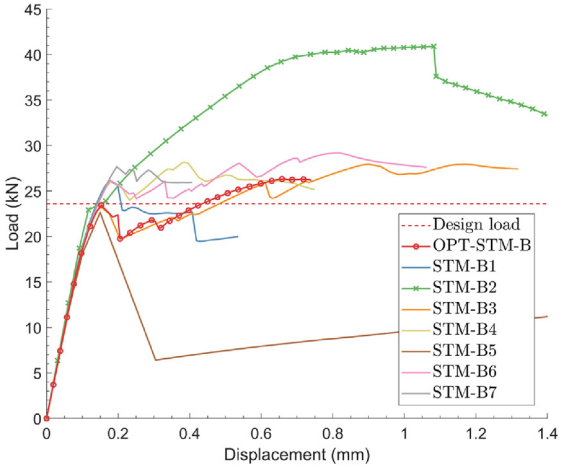

Fig. 39. The load-displacement curves for the STM models of Case B (irregular deep beam).

Table 9
The ultimate load and steel usage of STM models of the Case B (irregular deep beam).

Cases	Peak load (kN)	Steel volume (mm^3)	*PV* (%)
OPT-STM-B	26.51	24467	**59.4**
STM-B1	26.80	42715	34.38
STM-B2	40.90	152440	**14.7**
STM-B3	27.95	39994	38.3
STM-B4	28.12	43657	35.4
STM-B5	22.63	73639	16.8
STM-B6	29.18	27378	58.4
STM-B7	27.68	42554	35.6

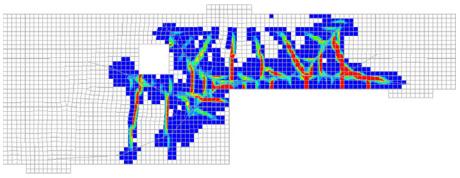

(a) Dapped-end beam

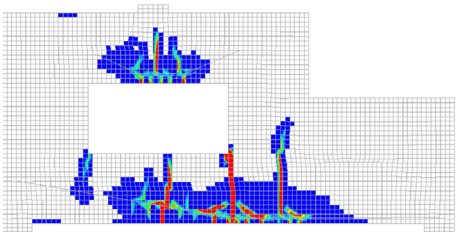

(b) Irregular deep beam

Fig. 40. Crack plots for the OPT-STM models at the ultimate state.

designs of OPT-STM-B and STM-B3 exhibit restabilization after the occurrence of critical cracks in the first peak load point. All models have a similar stiffness before developing the initial cracks. Only the designs of OPT-STM-B and STM-B1 reach the peak load at the moment of steel rupturing. Other models show ductility after reaching the peak load. In terms of steel economy and avoiding an overly conservative design, the automatically generated OPT-STM-B model outperforms both hand-tuned designs based on TO results, as well as all other STM models proposed for this problem. It is also noted, that through the very efficient use of steel, less ductile behavior is observed.

Based on evaluation results of two D-region problems under considered concrete and steel properties, large *PV* ratios are found for the generated OPT-STM model. Moreover, the resulting design reaches the peak load in the ultimate state, in which the structure fails due to steel rupturing. This indicates that more suitable STM models are generated, which are more accurate in representing the force flows in the D-region. Comparing TO inspired STM models (STM-A4 and STM-B6) with other manually created models, it is clear that the topology inspired models have relatively large *PV* ratios. However, by avoiding the manual interpretation of TO results, the *PV* ratios are most improved in the generated OPT-STM models. The crack plots of the two OPT-STM models are presented in Fig. 40. The OPT-STM models lead to flexural failure modes due to rupture of the reinforcement. By using a more suitable STM model, the usage of reinforcements is reduced and a more accurate design model for D-regions is obtained.

6. Conclusion

In this paper, a method is proposed to automatically generate optimization-based Strut-and-Tie (OPT-STM) models. In order to generate suitable models for the STM method, the proposed method includes three phases. The topology optimization results of the compliance minimization problem are obtained in the first phase. Next, in the topology extraction phase, truss-like structures which represent the TO results are generated. Finally, in the shape optimization phase, the requirements of the STM method on the axial-force equilibrium and geometrical conditions such as openings and cover thicknesses are considered. The entire procedure, depending on the selected resolution, typically produces a valid OPT-STM model in a few minutes.

In order to evaluate the generated OPT-STM models, in this study NLFEA is used to simulate the structural performance. Steel usage, peak loads and failure modes are used to evaluate the suitability of the used STM models. Based on obtained steel usage and peak loads, the *PV* ratio is defined to quantify the degree of utilization of steel reinforcement for further comparison. Two D-region design cases are investigated. In addition to two generated OPT-STM models, 11 STM models from previous studies are evaluated. Based on the present investigation, the conclusion is summarized as follows:

1. The proposed method successfully generates valid OPT-STM models for D-regions automatically and without manual adjustments. Recommendations for the settings of several parameters are provided based on parameter studies.
2. Detailed NLFEA simulation of RC structures based on OPT-STM models show a high stiffness and sufficient, yet not overly conservative load capacity. Compared with manually generated STM models, the OPT-STM models lead to the most economical steel usage relative to load capacity. The desired flexural failure mode is obtained.
3. Given these findings, the proposed STM generation method can be recommended for practical use. It removes variability due to manual STM model construction from the design process and replaces this with safe and economical designs. When implemented in the engineering practice, significant savings in design time and steel usage can be expected.

Declaration of Competing Interest

The authors declare that they have no known competing financial interests or personal relationships that could have appeared to influence the work reported in this paper.

Acknowledgments

The authors would like to thank Prof. Svanberg from KTH, Sweden for providing access to the MMA codes. The authors would like to thank the Editor and the anonymous reviewers for their constructive comments and valuable suggestions to improve the quality of the article.

References

[1] AASHTO. LRFD bridge design specifications, 7th ed. Washington, DC: AASHTO (American Association of State Highway and Transportation Officials); 2014.
[2] ACI. Building code requirements for structural concrete and commentary. Farmington Hills, MI: American Concrete Institute; 2014.
[3] Ali MA, White RN. Formulation of optimal strut-and-tie models in design of reinforced concrete structures. ACI Spec Publ 2000;193:979–98.
[4] Ali MA, White RN. Automatic generation of truss model for optimal design of reinforced concrete structures. Struct J 2001;98:431–42.
[5] Almeida VS, Simonetti HL, Neto LO. Comparative analysis of strut-and-tie models using Smooth Evolutionary Structural Optimization. Eng Struct 2013;56:1665–75.
[6] Alshegeir A, Ramirez J. Computer graphics in detailing strut-tie models. J Comput Civ Eng 1992;6:220–32.

[7] Bakir PG, Boduroglu HM. Mechanical behaviour and non-linear analysis of short beams using softened truss and direct strut & tie model. Eng Struct 2005;27:639–51.
[8] Belletti B, Damoni C, Hendriks MA. Development of guidelines for nonlinear finite element analyses of existing reinforced and pre-stressed beams. Eur Environ Civ Eng 2011;15:1361–84.
[9] Bendsøe MP, Kikuchi N. Generating optimal topologies in structural design using a homogenization method. Comput Methods Appl Mech Eng 1988;71:197–224.
[10] Bendsoe MP, Sigmund O. Topology optimization: theory, methods, and applications. New York: Springer; 2003.
[11] Biondini F, Bontempi F, Malerba PG. Optimal strut-and-tie models in reinforced concrete structures. Comput Assisted Mech Eng Sci 1999;6:280–93.
[12] Biondini F, Bontempi F, Malerba PG. Stress path adapting strut-and-tie models in cracked and uncracked RC elements. Struct Eng Mech 2001;12:685.
[13] Bruggi M. Generating strut-and-tie patterns for reinforced concrete structures using topology optimization. Comput Struct 2009;87:1483–95.
[14] Bruggi M. On the automatic generation of strut and tie patterns under multiple load cases with application to the aseismic design of concrete structures. Adv Struct Eng 2010;13:1167–81.
[15] Bruggi M. A numerical method to generate optimal load paths in plain and reinforced concrete structures. Comput Struct 2016;170:26–36. https://doi.org/10.1016/j.compstruc.2016.03.012.
[16] BSI. BS 8110-1: 1997 Structural use of concrete - Part 1: Code of practice for design and construction. London; 1997.
[17] CEN. Eurocode 2: Design of concrete structures-Part 1-1: General rules and rules for buildings. EN1992-1-1, Brussels; 2017.
[18] Chen BS, Hagenberger MJ, Breen JE. Evaluation of strut-and-tie modeling applied to dapped beam with opening. Struct J 2002;99:445–50.
[19] Chen H, Yi WJ, Hwang HJ. Cracking strut-and-tie model for shear strength evaluation of reinforced concrete deep beams. Eng Struct 2018;163:396–408.
[20] Chou YH, Lin CY. Improved image interpreting and modeling technique for automated structural optimization system. Struct Multidiscipl Optimiz 2010;40:215–26.
[21] CSA. Design of concrete structures. Rexdale, Ontario: Canadian Standards Association; 2004.
[22] Cuillière JC, François V, Nana A. Automatic construction of structural CAD models from 3D topology optimization. Comput-Aided Des Appl 2018;15:107–21.
[23] Du Z, Zhang W, Zhang Y, Xue R, Guo X. Structural topology optimization involving bi-modulus materials with asymmetric properties in tension and compression. Comput Mech 2019;63:335–63.
[24] El-Metwally S, Chen WF. Structural concrete: strut-and-tie models for unified design. CRC Press; 2017.
[25] El-Mezaini N, Çitipitioglu E,. Finite element analysis of prestressed and reinforced concrete structures. J Struct Eng 1991;117:2851–64. https://doi.org/10.1061/(ASCE)0733-9445(1991)117:10(2851).
[26] fib. Practitioners guide to finite element modelling of reinforced concrete structures. State-of-Art Report. CEB-FIB bulletin 45, Lausanne, Switzerland; 2008.
[27] Fib. fib Model Code for Concrete Structures 2010. Lausanne, Switzerland: Ernst & Sohn, Wiley; 2013. doi: 10.1002/9783433604090.
[28] Gaynor AT, Guest JK, Moen CD. Reinforced concrete force visualization and design using bilinear truss-continuum topology optimization. J Struct Eng 2013;139:607–18. https://doi.org/10.1061/(ASCE)ST.1943-541X.0000692.
[29] Geevar I, Menon D. Strength of reinforced concrete pier caps-experimental validation of strut-and-tie method. ACI Struct J 2019;116:261.
[30] Guan H. Strut-and-tie model of deep beams with web openings-an optimization approach. Struct Eng Mech 2005;19:361–80.
[31] Hanoon AN, Jaafar MS, Hejazi F, Aziz FNAA. Strut effectiveness factor for reinforced concrete deep beams under dynamic loading conditions. Case Stud Struct Eng 2016;6:84–102.
[32] Herranz UP, Maria HS, Gutiérrez S, Riddell R. Optimal Strut-and-Tie models using full homogenization optimization method. ACI Struct J 2012;109:605–14.
[33] Hsu MH, Hsu YL. Interpreting three-dimensional structural topology optimization results. Comput Struct 2005;83:327–37.
[34] Hwang SJ, Lee HJ. Strength prediction for discontinuity regions by softened strut-and-tie model. J Struct Eng 2002;128:1519–26.
[35] Jewett JL, Carstensen JV. Experimental investigation of strut-and-tie layouts in deep RC beams designed with hybrid bi-linear topology optimization. Eng Struct 2019;197:109322.
[36] Jewett JL, Carstensen JV. Topology-optimized design, construction and experimental evaluation of concrete beams. Autom Constr 2019;102:59–67.
[37] Karthik MM, Mander JB, Hurlebaus S. Displacement-based compatibility strut-and-tie method and application to monotonic and cyclic loading. J Struct Eng 2016;142:4016010.
[38] Kuchma D, Yindeesuk S, Nagle T, Hart J, Lee HH. Experimental validation of strut-and-tie method for complex regions. ACI Struct J 2008;105:578–89.
[39] Kwak HG, Noh SH. Determination of strut-and-tie models using evolutionary structural optimization. Eng Struct 2006;28:1440–9.
[40] Leu LJ, Huang CW, Chen CS, Liao YP. Strut-and-tie design methodology for three-dimensional reinforced concrete structures. J Struct Eng 2006;132:929–38.
[41] Ley MT, Riding KA, Bae S, Breen JE, et al. Experimental verification of strut-and-tie model design method. ACI Struct J 2007;104:749–55.
[42] Liang QQ, Xie YM, Steven GP. Topology optimization of strut-and-tie models in reinforced concrete structures using an evolutionary procedure. ACI Struct J 2000;97:322–32.
[43] Lin CY, Chao LS. Automated image interpretation for integrated topology and shape optimization. Struct Multidiscipl Optimiz 2000;20:125–37.
[44] Marti P. Basic tools of reinforced concrete beam design. J Proc 1985;82:46–56.
[45] Moradi M, Esfahani MR. Application of the strut-and-tie method for steel fiber reinforced concrete deep beams. Constr Build Mater 2017;131.
[46] Nielsen MP. Limit analysis and concrete plasticity. Englewood Cliffs, New Jersey: Prentice Hall, Inc; 1984.
[47] Oviedo R, Gutiérrez S, Santa Maria H. Experimental evaluation of optimized strut-and-tie models for a dapped beam. Struct Concr 2016;17:469–80.
[48] Park JW, Yindeesuk S, Tjhin T, Kuchma D. Automated finite-element-based validation of structures designed by the strut-and-tie method. J Struct Eng 2010;136:203–10.
[49] Quintero-Febres CG, Parra-Montesinos G, Wight JK. Strength of struts in deep concrete members designed using strut-and-tie method. ACI Struct J 2006;103:577.
[50] Reineck KH. Examples for the Design of Structural Concrete with Strut-and-Tie Mode, vol. 208. Farmington Hills (MI); 2002.
[51] Schlaich J, Schafer K. Design and detailing of structural concrete using strut-and-tie models. Struct Eng 1991;69:113–25.
[52] Schlaich J, Schafer K, Jennewein M. Toward a Consistent Design of Structural Concrete. PCI J 1987;32:74–150. https://doi.org/10.15554/pcij.05011987.74.150.
[53] Sigmund O, Petersson J. Numerical instabilities in topology optimization: A survey on procedures dealing with checkerboards, mesh-dependencies and local minima. Struct Optimiz 1998;16:68–75. https://doi.org/10.1007/BF01214002.
[54] Su RKL, Chandler AM. Design criteria for unified strut and tie models. Prog Struct Mat Eng 2001;3:288–98.
[55] Svanberg K. The method of moving asymptotes - a new method for structural optimization. Int J Numer Meth Eng 1987;24:359–73. https://doi.org/10.1002/nme.1620240207.
[56] Tjhin TN, Kuchma DA. Integrated analysis and design tool for the strut-and-tie method. Eng Struct 2007;29:3042–52.
[57] Vecchio FJ, Collins MP. Compression response of cracked reinforced concrete. J Struct Eng 1993;119:3590–610.
[58] Victoria M, Querin OM, Marti P. Generation of strut-and-tie models by topology design using different material properties in tension and compression. Struct Multidiscipl Optimiz 2011;44:247–58. https://doi.org/10.1007/s00158-011-0633-z.
[59] Xia Y, Langelaar M, Hendriks MAN. A critical evaluation of topology optimization results for strut-and-tie modeling of reinforced concrete. Comput Aided Civ Inf. 2020:1–20. https://doi.org/10.1111/mice.12537.
[60] Yi G, Kim NH. Identifying boundaries of topology optimization results using basic parametric features. Struct Multidiscipl Optimiz 2017;55:1641–54.
[61] Yin G, Xiao X, Cirak F, Topologically robust CAD model generation for structural optimisation; 2019. arXiv preprint arXiv:1906.07631.
[62] Yu M, Li J, Ma G. Theorems of limit analysis. New York: Springer; 2009.
[63] Yun YM. Computer graphics for nonlinear strut-tie model approach. J Comput Civ Eng 2000;14:127–33.
[64] Yun YM, Chae HS, Kim B, Ramirez JA. Verification of three-dimensional grid strut-and-tie model approach in structural concrete. ACI Struct J 2018;115:27–40.
[65] Yun YM, Kim BH. Two-dimensional grid strut-tie model approach for structural concrete. J Struct Eng 2008;134:1199–214.
[66] Yun YM, Ramirez JA. Strength of struts and nodes in strut-tie model. J Struct Eng 1996;122:20–9.
[67] Zhang TY, Suen CY. A fast parallel algorithm for thinning digital patterns. Commun ACM 1984;27:236–9.
[68] Zhong JT, Wang L, Deng P, Zhou M. A new evaluation procedure for the strut-and-tie models of the disturbed regions of reinforced concrete structures. Eng Struct 2017;148:660–72. https://doi.org/10.1016/j.engstruct.2017.07.012.
[69] Zhou L, Liu Z, He Z. Elastic-to-plastic strut-and-tie model for deep beams. J Bridge Eng 2018;23:4018007.